AN(N)^{N}I model for stacking fault energies in magnesium

Martina Ruffino

supervised by
Prof. Tony PAXTON

22nd March 2018

This report offers a study on the validity of Ising-like models for the calculation of stacking fault energies in magnesium with ideal axial ratio. Expressions for the stacking fault energies in terms of the interaction coefficients between layers of atoms are derived. The interaction energies are expressed as functions of the energies of the perfect structures; these are then calculated through the use of atomistic simulations exploiting density functional theory, and values for the J-coefficients of the theory are obtained for various combinations of structures and including different numbers of neighbours. A main dependence of the stacking fault energies on first nearest neighbour interaction is evidenced, and a hierarchy of the energies is established. The discrepancies between results obtained from different combinations of structures are discussed, and uncertainties on the values are estimated. The model is then extended to a number of magnesium alloys, and results are compared with the literature. The efficiency of the model is discussed, as well as suggestions for future work.

CONTENTS

1. INTRODUCTION

First isolated by English scientist Sir Humphrey Davy in 1808, magnesium is a metallic element characterised by atomic number 12, atomic weight 24.312 and a close-packed hexagonal crystal structure [1]. Industrial interest in magnesium and its alloys has been growing for the past few years and continues to grow. The reasons for the widespread use of magnesium include first and foremost its light weight: it is in fact 30% less dense than aluminium and 75% less dense than steel; moreover, its alloys present remarkable properties such as high strength, good corrosion resistance and high versatility [1]. With a reputation of being highly flammable, magnesium has a melting point of 650 C, and while it is indeed flammable when in powdered form, bulk magnesium does not burn if it is not heated past its melting point. New applications for magnesium alloys may be found in the aircraft industry if current safety regulations are changed; testing and further research on this issue are ongoing. In addition, there is a growing number of applications of magnesium in the medical field; in particular, magnesium is non-toxic and present naturally in the human body, and can interestingly be used to make implants that degrade spontaneously through corrosion, eliminating the need for surgery to remove them [2].

In this context, research on the mechanical properties of magnesium and its alloys is of primary importance. Stacking faults are crystal defects characterised by the misplacement of crystallographic planes with respect to the periodic stacking sequence of the crystal; knowledge of their energies constitutes a useful tool in understanding the plastic deformation mechanisms of metals [3]. In the literature, research on Mg SFEs has relied heavily on first-principle calculations based on density functional theory [4], with the main approach being that of the supercell method [5]. An alternative method is based on the $AN(N)^N I$ model, which was the focus of our research.

The aim of this report is then to assess the validity and efficiency of the $AN(N)^N I$ model for the calculation of stacking fault energies in magnesium. We first offer an overview of the background theory used throughout our research, concentrating on close-packed crystals, stacking faults and their description via Ising-like models, as well as an introduction to density functional theory. In the methods section, an account of the computational methods used is given, including an explanation of how density functional theory is implemented in the program we use. Moreover, in the results and analysis section of this report we state the results of our calculations, conducting an analysis through comparison with the literature and discussing the validity of the model used. Finally, we present suggestions for future work as well as the conclusions drawn from the research.

2. BACKGROUND THEORY

In the following section, we are going to outline an Ising-like description of crystals and planar stacking faults, showing how their energies can be calculated. We will then give an introduction on electronic structure and the density functional theory used to calculate the ground state energies of the metals, in order to give insight into the computational methods used in the present research.

I. Close-packed crystal structures

We are firstly going to give an overview on crystal structure and crystal geometry, in particular that of close-packed structures.

Mathematically, close-packing in two dimensions is defined as circles being arranged such that each has at least three contacts in the plane and not all of these fall in the same semicircle [6]. In this regard, the maximum number of nearest neighbours a circle can have is six; therefore the hexagonal packing of circles in the plane is the closest possible planar packing [6]. This easily seen in figure 1. Close-packing can be generalised to three dimensions; for spheres to be close-packed, each of them needs to have at least four points of contact with neighbouring spheres and not all of there fall in the same hemisphere [6]. In cubic closest packing, i. e. the fcc (face-centred cubic) structure, each sphere has twelve neighbours; this is the closest possible packing of spheres. However twelve spheres can be arranged to touch a single one in an infinite number of ways; therefore it has not been proved that this is the closest possible packing of spheres which fill space. Two structures which achieve close-packing of planes of spheres are the above mentioned fcc and the hcp (hexagonal close-packed) structures.
If we have hexagonal close-packed layers, these can be stacked on top of each other to obtain a three dimensional structure; in order for the structure to remain close-packed, the layers can be piled in two ways, which can be most easily illustrated through figure 1.
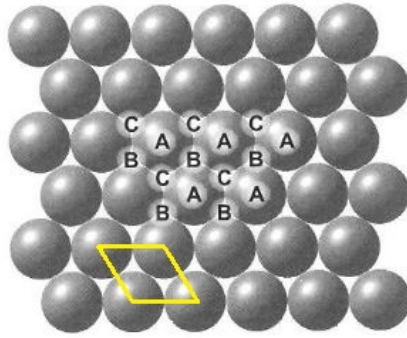

FIG. 1. This figure [7] shows how hexagonal layers of atoms can be stacked onto one another; if the first layer is called A, the second layer will be called B or C according to its position. The area outlined yellow is the surface area of the hcp unit cell.

The first layer of spheres is called A. We see that the next hexagonal layer can have two different positions: if the spheres are positioned in between the spheres that form empty upside triangles, the layer is called B; if they are above the downside triangles, the layer is called C [7]. It is readily seen that in this way each sphere will touch twelve neighbours, three being underneath it, six being abound it and three being above it. This shows again that there is more than one way to arrange spheres so

that they touch twelve neighbours, as discussed above.

A. The hcp structure

Through the stacking sequence of the layers, we can describe crystal structures in a simple way. In the simplest stacking sequence, the third layer is be directly above the first one, producing the sequence ABABAB..., which is the hcp structure [6–9] shown in figure. We can now define the unit cell; the one containing the smallest possible number of atoms needed to produce the whole structure (or the *primitive unit cell*) is the one in figure.
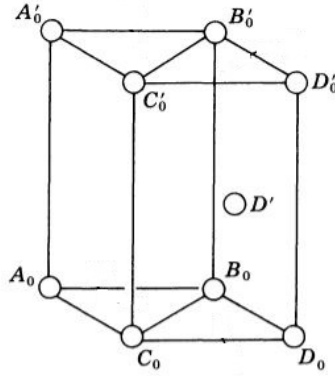

FIG. 2. This figure [10] shows the unit cell for the hcp structure.

This is expressed mathematically by the three lattice vectors, $\mathbf{a}_1$, $\mathbf{a}_2$ and $\mathbf{a}_3$: given the positions of the two atoms in the primitive unit cell, the positions of all the other atoms in the crystal will be at

$$\mathbf{r} = x\mathbf{a}_1 + y\mathbf{a}_2 + z\mathbf{a}_3$$

where x, y, z are integer numbers. The atom positions can be given in cartesian coordinates or, once the lattice vectors have been specified, in fractional coordinates, i. e. using the lattice vectors as a coordinate system. For example, for the hcp primitive unit cell, a possible set of lattice vectors, in units of a, the lattice constant, is the following:

$$\mathbf{a}_1 = [1, 0, 0]$$
$$\mathbf{a}_2 = \left[-\frac{1}{2}, \frac{\sqrt{3}}{2}, 0 \right]$$
$$\mathbf{a}_3 = [0, 0, q]$$

where $\hat{\mathbf{i}}, \hat{\mathbf{j}}$ and $\hat{\mathbf{k}}$ are the cartesian unit vectors. The atom positions then are:

	cartesian	fractional
atom 1	[0, 0, 0]	[0, 0, 0]
atom 2	$[\frac{1}{2}, \frac{\sqrt{3}}{6}, \frac{q}{2}]$	$[\frac{2}{3}, \frac{1}{3}, \frac{1}{2}]$

5

Here $q = \frac{c}{a}$ is the axial ratio, with c being the height of the unit cell. It is readily seen that if a is twice the radius of an atom, then for the atoms to be close-packed the height of the unit cell has to be $c = 4\sqrt{\frac{2}{3}}r$, resulting in the axial ratio being $\frac{c}{a} = \sqrt{\frac{8}{3}} = 1.633$, which is the *ideal axial ratio*. In the case of real crystals, some have axial ratios that come close to ideal, such as magnesium (Mg) (1.626), which will be the object of our study. However, some elements have axial ratios that are quite far from ideal, and this is an indicator of the fact that bonding between atoms also depends on other factors.

B. The fcc structure

Another common stacking sequence is ABC; this sequence corresponds to the fcc structure [7–9], which can be described in a simpler way than by looking at the stacking of layers. In fact, as the name of the structure suggests, the fcc is a cubic structure; one of its possible unit cell is a cube with an atom at each corner and one at the centre of each face. The fcc structure then belongs to cubic close-packed structures. A prominent feature of the fcc structure is that all the atoms have equivalent environments, and thus the primitive unit cell contains only one atom, as can be seen from figure 3.
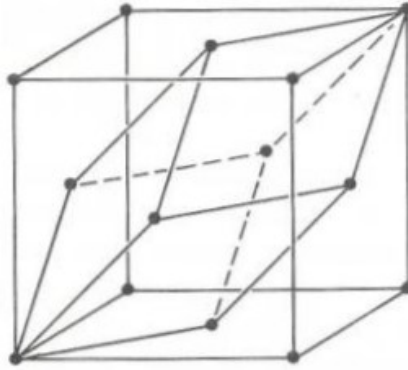

FIG. 3. This figure [6] shows the face-centered cubic (fcc) structure. The primitive unit cell is outlined inside the conventional unit cell.

For the primitive unit cell, the lattice vectors are, in units of the lattice constant a,

$$\mathbf{a}_1 = \left[0, \frac{1}{2}, \frac{1}{2}\right]$$
$$\mathbf{a}_2 = \left[\frac{1}{2}, 0, \frac{1}{2}\right]$$
$$\mathbf{a}_3 = \left[\frac{1}{2}, \frac{1}{2}, 0\right]$$

C. Other close-packed structures

The number of possible close-packed structures is potentially very large. We will give a brief description of three more structures, as we used in our calculations a total of five structures to obtain expressions for the stacking fault energies of magnesium.

Firstly we shall introduce some useful notation to identify the structures. We label each structure with a number, representing the number of layers in the unit cell, followed by a letter, representing the Bravais lattice type; this notation is known as the Ramsdell classification [11]. For example, the hcp structure will be called "2H", since its periodicity is defined by two layers and its lattice is hexagonal, whereas the fcc structure is called 3C, C standing for cubic. This notation is used to easily identify structures with more complex periodic stacking sequences, called polytypes, and it comes to us from the polytypes of silicon carbide (SiC) in [12].

The third structure we have chosen is the double-hcp, or 4H, which contains 4 atoms in the unit cell. Its stacking sequence is ABCB. There are then the 6H structure, with stacking ABCACB, and the 9R structure, where R stands for rhombohedral, with stacking ABCBCACAB [13]. The following table summarises the lattice vectors and atom positions (in fractional coordinates) of the three structures, in units of a (the lattice constant); q is the axial ratio of the hcp structure.

structure	lattice vectors	atom positions
4H	$\mathbf{a}_1 = [1,0,0] \, \mathbf{a}_2 = [-\frac{1}{2}, \frac{\sqrt{3}}{2}, 0] \, \mathbf{a}_3 = [0,0,2q]$	$[0,0,0][\frac{2}{3}, \frac{1}{3}, \frac{1}{4}][0,0,\frac{1}{2}][\frac{1}{3}, \frac{2}{3}, \frac{3}{4}]$
6H	$\mathbf{a}_1 = [1,0,0] \, \mathbf{a}_2 = [-\frac{1}{2}, \frac{\sqrt{3}}{2}, 0] \, \mathbf{a}_3 = [0,0,3q]$	$[0,0,0][\frac{2}{3}, \frac{1}{3}, \frac{1}{6}][\frac{1}{3}, \frac{2}{3}, \frac{1}{3}]$
		$[0,0,\frac{1}{2}][\frac{1}{3}, \frac{2}{3}, \frac{2}{3}][\frac{2}{3}, \frac{1}{3}, \frac{5}{6}]$
9R	$\mathbf{a}_1 = [1,0,0] \, \mathbf{a}_2 = [-\frac{1}{2}, \frac{\sqrt{3}}{2}, 0] \, \mathbf{a}_3 = [0,0,9q]$	$[0,0,0][\frac{1}{3}, \frac{2}{3}, \frac{1}{9}][\frac{2}{3}, \frac{1}{3}, \frac{2}{9}]$
		$[\frac{1}{3}, \frac{2}{3}, \frac{1}{3}][\frac{2}{3}, \frac{1}{3}, \frac{4}{9}][0,0,\frac{5}{9}]$
		$[\frac{2}{3}, \frac{1}{3}, \frac{2}{3}][0,0,\frac{7}{9}][\frac{1}{3}, \frac{2}{3}, \frac{8}{9}]$

II. Stable stacking faults in the basal plane

Having introduced close-packing, we can now introduce the topic that is the main focus of our research, i. e. stacking faults. In the type of structure described above, a stacking fault is obtained when the periodicity of the structure is somewhat interrupted and modified. For the case of a hcp structure such as Magnesium, the close-packed planes are (0002) planes, i.e. basal planes [10]; in this report we will then discuss stacking faults in the basal plane. In addition, all the faults that we are going to describe locate at stable sites, hence the label "stable stacking fault energies" [3]; an unstable stacking fault energy also exists, and it is defined as the maximum energy barrier hindering one half of the crystal when sliding above the other half along the slip plane [14].

There are three types of stable stacking faults: in the intrinsic faults the normal stacking sequence is preserved on either side of the fault up to the fault plane [10]; in faults of the extrinsic type an extra plane is inserted that does not follow the correct stacking sequence of the crystal, on both sides of the fault. A third type is the twin-like fault, whose peculiarity is to possess mirror symmetry about the fault plane [5].

In the case of hcp, there are two intrinsic faults. I_1, also called the growth fault, is obtained through the removal of a plane from the perfect hcp structure, followed by the shear of the crystal above the fault of $\frac{1}{3}$ in the $[\bar{1}100]$ direction, as follows

$$...ABAB... \rightarrow ...ABABBAB... \rightarrow ...ABABCBCB...$$

[3]. In analogy to the definition given by Denteneer and van Haeringen in [15], the I_1 stacking fault can be represented as the limiting structure of a polytype with repeat unit $ABC(BC)^n(n = 0, 1, 2, ...)$ consisting of N layers in the limit $N \to \infty$. I_2, or deformation fault, can be formed directly by a shear of $\frac{1}{3}$ in the $[\bar{1}100]$ direction, i.e.

$$...ABABAB... \to ...ABAAB... \to ...ABABCACA...$$

[10]. Again, this fault can be represented by a polytype with repeat unit $ABC(AC)^m(m = 0, 1, 2, ...)$ made up of M layers, in the limit $M \to \infty$.

There is one extrinsic fault, E, which is formed by inserting an extra plane (a C plane) in the perfect sequence, producing

$$...ABABAB... \to ...ABACAB...$$

[10]. In this case the polytype has repeat unit $ABAC(AB)^l(l = 0, 1, 2, ...)$, with L layers, in the limit $L \to \infty$.

Finally, the twin-like fault, T_2, is formed by replacing an A plane with a C plane, yielding

$$...ABABAB... \to ...ABABCBABA...$$

[3], and it may be represented as a polytype with repeated unit $ABC(BA)^k(k = 0, 1, 2, ...)$ consisting of K layers, in the limit $K \to \infty$.

III.   The AN(N)^{N}I model

Now that we have a geometric description of the structures we have used in our work, we can introduce the theory that has been the focus of our research, that is, an Ising-like description of the structural energy for solids. The Ising model [16] in one dimension gives an expression for the energy of an array of magnetic moments placed with equal spacing. Each moment is represented by a spin, which can be pointing up or down, and consequently have value $\sigma = \pm 1$. In the case where no external magnetic field is applied, the energy of the array of moments is given by the interaction energy between the moments. The hamiltonian of the system is the following:

$$H = -J \sum_{i=1}^{N} \sigma_i \sigma_{i+1}$$

Assuming that the strength of the interaction decays very quickly when the distance is increased, the simplest model accounts for nearest neighbour interaction only; therefore the interaction energy has a fixed value J. The total energy decreases when two neighbouring spins have the same sign, and increases when they have opposite sign, hence the minus sign.

This can be generalised to include interactions between further neighbours by introducing another index j:

$$H = -\sum_{i,j}^{N} J_j \sigma_i \sigma_{i+j}$$

8

So that now the coefficients J_j represent the interaction energies between first nearest neighbours, second nearest neighbours and so on.

Following Denteneer and van Haeringen in [15], we will apply this model to crystals by looking at them as layers of atoms stacked onto one another and defining the structural energy as the sum of the interaction energies between layers plus a contribution coming from the energy of the system when interactions are not considered.

We assign a spin $S = \pm 1$ to the ith layer, according to whether the layer $i+1$ follows the "correct" stacking sequence or not [15]. Conventionally, we assert that the correct stacking sequence is ABC, whereas the incorrect one is CBA. For example, if a layer A is followed by a layer B, its spin is $+1$; on the other hand, if it is followed by a C layer its spin is -1. Consequently, the energy of a crystal with an arbitrary stacking sequence is expressed as follows:

$$E = E_0 - \sum_{n}^{N-1} J_n \sum_{i}^{N} S_i S_{i+n} \tag{1}$$

with E_0 being the energy of the system when all interactions between layers are ignored and N being the number of layers. Just like in the Ising model for magnetic moments, the assumption here is that the magnitude of the interaction energy between layers decreases as n increases. In the ANNNI (Axial Next Nearest Neighbour Ising) model [17] only interactions up to J_2 are included; in our work, we proposed to observe the behaviour of the J parameters as further neighbours are taken into account, effectively using the AN(N)^{N}I model(s), with $N = 1, 2, 3, 4$ depending on how may neighbours are taken into account; for this reason, we will include in our equations terms of order up to J_4.

For a periodic arrangements of layers, the evaluation of the sums is straightforward. Normalising the energies to the number of layers, we derive expressions for the energies per unit cell of the five polytypes we have listed using 1, as per in [15]:

$$E_{3C} = J_0 - J_1 - J_2 - J_3 - J_4 \tag{2}$$

$$E_{2H} = J_0 + J_1 - J_2 + J_3 - J_4 \tag{3}$$

$$E_{4H} = J_0 + J_2 - J_4 \tag{4}$$

$$E_{6H} = J_0 - \frac{1}{3}J_1 + \frac{1}{3}J_2 + J_3 + \frac{1}{3}J_4 \tag{5}$$

$$E_{9R} = J_0 + \frac{1}{3}J_1 + \frac{1}{3}J_2 - J_3 + \frac{1}{3}J_4 \tag{6}$$

where J_0 is the energy of one layer if interactions are not taken into account. Equations 2 to 6 can be rearranged to find the interaction energy coefficients in terms of the energies of the perfect structures; however it should be noted that this can only be done if the structures are close-packed and the volume of the unit cell is kept constant. In fact this ensures that the distance between neighbouring atoms is the same in all the structures, and so are the J-parameters.

The energies of four structures containing a stable stacking fault in the basal plane each can also be expressed in these terms, as a function of the number of layers; this was done, for example, by Hu and

Yang in [18], and is easily reproducible:

$$E_{I_1}(N) = J_0 + \frac{N-2}{N}J_1 - \frac{N-4}{N}J_2 + \frac{N-6}{N}J_3 - \frac{N-8}{N}J_4 \tag{7}$$

$$E_{I_2}(N) = J_0 + \frac{N-4}{N}J_1 - \frac{N-4}{N}J_2 + \frac{N-4}{N}J_3 - \frac{N-4}{N}J_4 \tag{8}$$

$$E_{E}(N) = J_0 + \frac{N-6}{N}J_1 - \frac{N-4}{N}J_2 + \frac{N-6}{N}J_3 - \frac{N-8}{N}J_4 \tag{9}$$

$$E_{T_2}(N) = J_0 + \frac{N-4}{N}J_1 - \frac{N-8}{N}J_2 + \frac{N-8}{N}J_3 - \frac{N-8}{N}J_4 \tag{10}$$

The energies of the stacking faults are then as defined in Denteneer and van Haeringen, i.e. as the excess energy compared to the perfect crystal:

$$\Delta E_{SFE} = \lim_{N \to \infty} 2N[E_{SFE}(2N) - E_{hcp}] \tag{11}$$

Where $2N$ is the periodicity of the crystal.

Applying this to eqs. 7 to 10, we obtain

$$\Delta E_{I_1} = -2J_1 + 4J_2 - 6J_3 + 8J_4 \tag{12}$$

$$\Delta E_{I_2} = -4J_1 + 4J_2 - 4J_3 + 4J_4 \tag{13}$$

$$\Delta E_{E} = -6J_1 + 4J_2 - 6J_3 + 8J_4 \tag{14}$$

$$\Delta E_{T_2} = -4J_1 + 8J_2 - 8J_3 + 8J_4 \tag{15}$$

as found by ref [19] and ref [18] as well. However, the J-parameters can be expressed in terms of the energies of the perfect structures; we have therefore found a way to calculate the stacking fault energies indirectly, without having to compute the energies of the structures containing the faults, a process that can often be computationally demanding. Finally, the stacking fault energy is usually expressed as energy per unit area [15]; therefore it is defined in the literature as

$$\gamma = \frac{\Delta E}{A} \tag{16}$$

where A is the area that defines the unit cell in one layer [15]; in the case of hcp, this is $A = \frac{\sqrt{3}}{2}a^2$ with a the lattice constant.

IV.   Density Functional Theory

Having described how the AN(N)^{N}I model provides an expression for the stacking fault energies that depends solely on the structural energies of perfect crystals, we shall now concentrate on how these energies are calculated in practice. Being interested in the ground state energies of crystals, we were able to use the density functional theory, which is a rather powerful approach to the quantum theory of electronic structure of matter [20]. Density functional theory (from now on DFT) [20–22] allows to substitute the wave function of the system with the electron density as the basic variable we will be working with, without loss of formality. In this section we will give a brief introduction on how this is done, while the methods chapter of this report will explain how DFT is implemented in the code we have used.

To begin with, we shall say a few words about units. In atomic physics literature, the most popular units are atomic units. In Hartree atomic units, $e = 1$, $m = 1$, $\hbar = 1$ and $4\pi\epsilon_0 = 1$, with m being the mass of the electron and e its charge; in this convention, energy is expressed in *hartrees*. In Rydberg atomic units, $\hbar = 1$, $2m = 1$, $e^2 = 2$ and $4\pi\epsilon_0 = 1$, so that energy is expressed in *rydbergs*. In the derivation that follows, we have chosen to simply use $4\pi\epsilon_0 = 1$, and keep track of all other constants, as done in ref [22], whose derivation we are going to follow.

The hamiltonian for a system of N nuclei and n electrons is the following:

$$\hat{H} = \sum_{i=1}^{n} \left(-\frac{\hbar^2}{2m}\nabla_i^2 + v_{\text{ext}}(\mathbf{r}_i) \right) + \sum_{i<j} \frac{e^2}{|\mathbf{r}_i - \mathbf{r}_j|} = \hat{T} + \hat{V}_{en} + \hat{V}_{ee} \tag{17}$$

Where

$$v_{\text{ext}}(\mathbf{r}_i) = -\sum_{I=1}^{N} \frac{Z_I e^2}{|\mathbf{r}_i - \mathbf{R}_I|}$$

is the "external potential" acting on electron i, i. e. the potential due to the nuclei of charge Z_I [20]. The total electronic energy is then the expectation value of the hamiltonian, i. e. $\langle \Psi | \hat{H} | \Psi \rangle$, where $\Psi(s_1, \mathbf{r}_1, s_2, \mathbf{r}_2, ..., s_n, \mathbf{r}_n)$ is a normalised many-body wave function, and as such it is a function of all the electron coordinates and spins [22]. Normalisation implies that the sum of all probabilities amounts to 1:

$$1 = \int ds_1 d\mathbf{r}_1 ds_2 d\mathbf{r}_2 ... ds_n d\mathbf{r}_n |\Psi(s_1\mathbf{r}_1 s_2\mathbf{r}_2 ... s_n\mathbf{r}_n)|^2 \tag{18}$$

The probability that there is an electron in the volume elment $d\mathbf{r}_1$ is $\rho(\mathbf{r}_1)d\mathbf{r}_1$ and the charge density at $\mathbf{r}_1$ is

$$\rho(\mathbf{r}_1) \equiv n \int ds_1 ds_2 d\mathbf{r}_2 ... ds_n d\mathbf{r}_n |\Psi|^2 \tag{19}$$

The probability that there is an electron in $d\mathbf{r}_1$ *and* an electron in $d\mathbf{r}_2$ is $2\rho_2(\mathbf{r}_1\mathbf{r}_2)$, so that

$$2\rho_2(\mathbf{r}_1\mathbf{r}_2) \equiv n(n-1) \int ds_1 ds_2 ds_3 d\mathbf{r}_3 ... ds_n d\mathbf{r}_n |\Psi|^2 \tag{20}$$

ρ and ρ_2 are the only *density matrices* that we will need to calculate the expectation value of the hamiltonian, since $\hat{H}$ contains only one and two particle operators [22]. The total energy W is then defined as the zero temperature, ground state energy of the assembly of nuclei and electrons [22], and as such it is the sum of the electronic energy E and the repulsion energy between the nuclei

$$\hat{V}_{nn} = \sum_{I<J} \frac{Z_I Z_J e^2}{|\mathbf{R}_I - \mathbf{R}_J|} \tag{21}$$

so that

$$W = E + \hat{V}_{nn} \tag{22}$$

The wave function we introduced above is a many-body wave function; because we want to deal only with one-electron wave functions, we introduce the Hartree-Fock approximation [23], which allows us to approximate Ψ as an antisymmetrized (in order to obey Pauli's exclusion principle) product of

11

N orthonormal spin orbitals $\phi_i(\mathbf{r})$, each a product of a spatial orbital $\psi_k(\mathbf{r})$ and a spin function $\chi_i(s_j)$ [20]. This is the Slater determinant:

$$\Psi_{\text{HF}} = \frac{1}{\sqrt{n!}} \begin{vmatrix} \phi_1(s_1\mathbf{r}_1) & \phi_2(s_1\mathbf{r}_1) & \dots & \phi_n(s_1\mathbf{r}_1) \\ \phi_1(s_2\mathbf{r}_2) & \phi_2(s_2\mathbf{r}_2) & \dots & \phi_n(s_2\mathbf{r}_2) \\ \vdots & \vdots & \ddots & \vdots \\ \phi_1(s_n\mathbf{r}_n) & \phi_2(s_n\mathbf{r}_n) & \dots & \phi_n(s_n\mathbf{r}_n) \end{vmatrix} \tag{23}$$

According to the variational principle, the ground state energy of the system is always smaller than or equal to the expectation value of the hamiltonian:

$$E_{\text{HF}} = \langle \Psi_{\text{HF}} | \hat{H} | \Psi_{\text{HF}} \rangle \geq E_0 \tag{24}$$

Therefore we can vary the trial wave functions ϕ_i to minimise E_{HF}, and this will give us the ground state energy. Using 23 in 24, we obtain

$$E_{\text{HF}} = \sum_{i=1}^{n} h_i + \frac{1}{2} \sum_{i,j=1}^{n} (C_{ij} - A_{ij}) \tag{25}$$

with

$$h_i = \int \bar{\psi}_i(\mathbf{r}) \left[-\frac{\hbar^2}{2m} \nabla^2 + v_{ext} \right] \psi_i(\mathbf{r}) d\mathbf{r}$$

$$C_{ij} = \int \int |\psi_i(\mathbf{r}_1)|^2 \frac{e^2}{|\mathbf{r}_1 - \mathbf{r}_2|} |\psi_j(\mathbf{r}_2)|^2 d\mathbf{r}_1 d\mathbf{r}_2$$

$$A_{ij} = \delta_{s_i s_j} \int \int \bar{\psi}_i(\mathbf{r}_1) \psi_j(\mathbf{r}_1) \frac{e^2}{|\mathbf{r}_1 - \mathbf{r}_2|} \bar{\psi}_i(\mathbf{r}_2) \psi_j(\mathbf{r}_2) d\mathbf{r}_1 d\mathbf{r}_2$$

Here C_{ij} are called Coulomb integrals, and A_{ij} are the exchange integrals [20]. $C_{ii} = A_{ii}$, so that the sum in 25 can be run over all i and j, since all the electron self-interaction terms cancel. Moreover the single determinant form of Ψ_{HF} ensures that the exchange energy between two electrons with opposite spins vanishes, as is enforced by the delta function in A_{ij}.

The Coulomb term can be rewritten as

$$C[\rho] = \frac{1}{2} e^2 \int d\mathbf{r}_1 d\mathbf{r}_2 \frac{\rho(\mathbf{r}_1)\rho(\mathbf{r}_2)}{|\mathbf{r}_1 - \mathbf{r}_2|} \tag{26}$$

showing explicitly that this is the classical electrostatic energy of the electron distribution $\rho(\mathbf{r})$, or Hartree energy. This neglects fluctuations in the electron coordinates such that electrons repel each other; one of the reasons for this is the Pauli exclusion principle, which leads to the creation of an exchange hole that forms a neutral quasiparticle with the electron. Moreover, the Coulomb repulsion contributes to further deepening the hole. Due to this "correlated motion", the electron-electron interaction energy is actually smaller than the Hartree energy.

From 17 we can write the expectation value of $\hat{V}_{ee}$:

$$\langle \Psi | \hat{V}_{ee} | \Psi \rangle = \int \frac{e^2}{|\mathbf{r}_1 - \mathbf{r}_2|} \rho_2(\mathbf{r}_1 \mathbf{r}_2) d\mathbf{r}_1 \mathbf{r}_2 \tag{27}$$

This can be separated into the classical part ($C[\rho]$) and the part due to electron correlations. The pair distribution function is

$$g(\mathbf{r}_1\mathbf{r}_2) = \frac{2\rho_2(\mathbf{r}_1\mathbf{r}_2)}{\rho(\mathbf{r}_1)\rho(\mathbf{r}_2)}$$

So that comparing 26 and 27 we can write

$$\rho_2(\mathbf{r}_1\mathbf{r}_2) = \frac{1}{2}\rho(\mathbf{r}_1)\rho(\mathbf{r}_2)g(\mathbf{r}_1\mathbf{r}_2) = \frac{1}{2}\rho(\mathbf{r}_1)\rho(\mathbf{r}_2)[1 + h(\mathbf{r}_1\mathbf{r}_2)] \tag{28}$$

where we have defined the pair correlation function as $h(\mathbf{r}_1\mathbf{r}_2) = g(\mathbf{r}_1\mathbf{r}_2) - 1$, in order to correct 26 to account for electron correlations.

However the Hartree Fock approximation only takes into account the correlation of parallel spin electrons, and this interaction is known as exchange. To account for antiparallel spins a correlation interaction has been introduced, defined as

$$E_{\text{correlation}} = E_{\text{exact}} - E_{\text{HF}} \tag{29}$$

In order to include this error correction in our calculation, we will from now on refer to electron correlation as exchange and correlation; the exchange and correlation hole is neutral, so that the electron behaves as a neutral quasiparticle with increased effective mass, effectively constituting an independent particle when it carries an xc hole. In a non-uniform system the shape of the xc-hole will be quite different from spherical; however it can be shown that the xc energy is independent of the shape of the hole and depends only on its spherical average.

We now possess all the instruments we need to introduce density functional theory; this is firstly based on the two Hohenberg Kohn theorems [24]. The first theorem states that in the ground state the total energy is determined solely by a knowledge of the electron density $\rho(\mathbf{r})$. The second theorem states that for all densities $\tilde{\rho}(\mathbf{r}) \geq 0$ with $\int \tilde{\rho}(\mathbf{r})d\mathbf{r} = n$, $E[\tilde{\rho}(\mathbf{r})]$ is minimised by the ground state density $\tilde{\rho}(\mathbf{r}) = \rho(\mathbf{r})$, which corresponds to the variational principle. These two theorem allow us to calculate the ground state energy from the electron density only, without knowing the many-electron wave function, and to do so by minimising the energy functional with respect to all correctly normalised non negative densities [22]. Using 17 we can write

$$E[\rho] = T[\rho] + V_{en}[\rho] + V_{ee}[\rho] = F[\rho] + \int \rho(\mathbf{r})v_{\text{ext}}(\mathbf{r})d\mathbf{r} \tag{30}$$

Where the interaction with the external potential was taken out and $F[\rho] = \langle\Psi|\hat{T} + \hat{V}_{ee}|\Psi\rangle$ does not depend on v_{ext}. We can take out the part of V_{ee} that we have calculated, i. e. the classical self-energy of the electrons, and relegate everything else in a functional G:

$$F[\rho] = \frac{1}{2}e^2 \int d\mathbf{r}_1 d\mathbf{r}_2 \frac{\rho(\mathbf{r}_1)\rho(\mathbf{r}_2)}{|\mathbf{r}_1 - \mathbf{r}_2|} + G[\rho] = C + G \tag{31}$$

We now need to minimise $E[\rho]$ with respect to ρ; using $n = \int \rho(\mathbf{r})d\mathbf{r}$ and introducing a Lagrange undetermined multiplier, we get

$$\frac{\delta}{\delta\rho}\left\{E[\rho] - \mu\left(\int \rho(\mathbf{r}) - n\right)\right\} = 0$$

13

where $\frac{\delta}{\delta\rho}$ is the functional derivative. It can be shown that

$$\frac{\delta C}{\delta\rho}(\mathbf{r}_2) = e^2 \int \frac{\rho(\mathbf{r}_1)}{|\mathbf{r}_1 - \mathbf{r}_2|} d\mathbf{r}_1 = \phi_H \tag{32}$$

where ϕ_H is called the Hartree potential. Using 30 and 31 we now have

$$\frac{\delta E}{\delta\rho} = \mu = v_{\text{ext}} + \phi_H + \frac{\delta G}{\delta\rho} \tag{33}$$

which is known as the Euler-Lagrange equation [20], and where it can be shown that μ is the chemical potential. In order to solve the Euler-Lagrange equation, we are going to use the so-called "Kohn and Sham trick" [4]. Kohn and Sham realised that the form of equation 33 is the same as the equation for the ground state density of a system of non-interacting electrons subject to a potential v_0 [21]:

$$\mu_0 = v_0(\mathbf{r}) + \frac{\delta T_0}{\delta\rho} \tag{34}$$

where T_0 is the kinetic energy of a non-interacting electron gas of density ρ. To see this, we take out of $G[\rho]$ the kinetic energy of the non-interacting electron gas, and redefine the exchange and correlation energy, as follows:

$$G[\rho] = T_0[\rho] + E_{xc}[\rho] \tag{35}$$
$$E_{xc} = (T - T_0) + (V_{ee} - C) \tag{36}$$

where $(T - T_0)$ is essentially the interaction part of the kinetic energy. Now instead of v_0 we write an effective potential v_{eff}:

$$v_{\text{eff}}[\rho, \mathbf{r}] = v_{ext}(\mathbf{r}) + \phi_H(\mathbf{r}) + \frac{\delta E_{xc}}{\delta\rho} \tag{37}$$

So that 33 now has the same form as 34, whose solution is found by solving the "Kohn-Sham equations" (which are in direct analogy to the Schrödinger equation):

$$\left(-\frac{\hbar^2}{2m}\nabla^2 + v_{\text{eff}}[\rho, \mathbf{r}] \right)\phi_i(s\mathbf{r}) = \epsilon_i \phi_i(s\mathbf{r}) \tag{38}$$

with the electron density given by

$$\rho(\mathbf{r}) = \sum_{i=1}^{n}\sum_{s}|\phi_i(s\mathbf{r})|^2 \tag{39}$$

We have successfully managed to recast the many-electron problem into a product of one-electron problems. However, it should be noted that the eigenvalues and eigenvectors (the Kohn-Sham orbitals) of equation 38 are not the energies and wave functions of our system; in fact, they have physical meaning in the case of the non-interacting electron gas, because there the Hartree-Fock equations are exact, but in our case $V_{ee} \neq 0$ and while the ϕ_i give the correct density because they solve the correct Euler-Lagrange equation, they do not have a physical significance.

It is to be noted the working above is all exact; in order to solve the problem, we will need to make some approximations, and since the many-body terms have been relegated to the exchange and correlation energy, this is the quantity that we are going to approximate. Taking into account that i) the electron

together with its hole forms a neutral quasiparticle, ii) E_{xc} represents the short ranged part of V_{ee} and iii) it depends only on the spherical average of the xc-hole, we are going to use the local density approximation (LDA):

$$E_{xc}^{\text{LDA}}[\rho] = \int \epsilon_{xc}(\rho)\rho(\mathbf{r})d\mathbf{r} \tag{40}$$

where ϵ_{xc} is the *local* exchange and correlation energy density. We are asserting that the contribution to E_{xc} from point $\mathbf{r}$ is the xc-energy of a homogeneous electron gas with density $\rho(\mathbf{r})$. In other words, we treat the energy as a function of the local electron density and integrate over the system [21]. We now want to express 37 in the LDA, so we define an exchange and correlation potential as

$$\mu_{xc} \equiv \frac{\delta E_{xc}}{\delta\rho}$$
$$\mu_{xc}^{\text{LDA}} = \frac{d}{d\rho}(\rho\epsilon_{xc}(\rho)) \tag{41}$$

Then we solve the Poisson equation

$$\nabla^2\phi_H(\mathbf{r}) = 4\pi e^2\rho(\mathbf{r})$$

and find an expression for the effective potential. We plug this in the Kohn Sham equations 38. Since the potential itself depends on the density, the KS equations have to be solved self-consistently [21]: we guess an input density ρ_{in} from which we obtain a potential V_{in}; we use this to solve 37 and get an output density ρ_{out}, which is then used as the new input density for the next iteration, and the procedure is repeated until $\rho_{in} = \rho_{out}$. This is shown schematically in the diagram in figure 4.
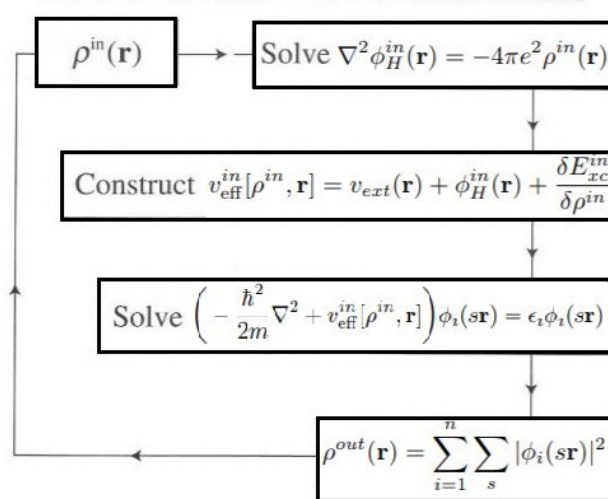

FIG. 4. This figure (adapted from [21]) shows a diagram of the self-consistent calculation.

Instead of solving the KS equations as differential equations, the standard approach is to expand the orbitals in a set of basis functions:

$$\phi_i(s\mathbf{r}) = \sum_{\alpha=1}^{M} c_{i\alpha}\sigma_\alpha(\mathbf{r})$$

15

We then find the matrix elements of $\hat{H}^{\text{eff}} = -\frac{\hbar^2}{2m}\nabla^2 + v_{\text{eff}}$, i. e. $H_{\alpha\beta} = \langle\sigma_\alpha|\hat{H}^{\text{eff}}|\sigma_\beta\rangle$ and the overlap $S_{\alpha\beta} = \langle\sigma_\alpha|\sigma_\beta\rangle$, so that the K-S equations are now a set of M algebraic equations

$$(\mathbf{H} - \epsilon_j\mathbf{S})\mathbf{c}_j = 0$$

from which we take the n eigenvalues and corresponding eigenvectors and

$$\rho(\mathbf{r}) = \sum_{i=1}^{n}\sum_s |\phi_i(s\mathbf{r})|^2 = \sum_{j \text{ occ.}}\sum_{\alpha\beta}\bar{c}_{j\alpha}S_{\alpha\beta}c_{j\beta}$$

At each iteration the total energy is

$$E[\rho_{out}] = T_0[\rho_{out}] + V_{en}[\rho_{out}] + C[\rho_{out}] + E_{xc}[\rho_{out}] \tag{42}$$

It can be shown, using equations 37, 32 and 41 , writing $\rho_{out} = \rho_{in} + \Delta\rho$ and Taylor expanding $E_{xc}[\rho_{out}]$ around $\Delta\rho$, that this corresponds to

$$E[\rho_{out}] = \sum_{j \text{ occ.}}\epsilon_j - \frac{1}{2}e^2\int\frac{\rho_{in}(\mathbf{r}_1)\rho_{in}(\mathbf{r}_2)}{|\mathbf{r}_1 - \mathbf{r}_2|}d\mathbf{r}_1 d\mathbf{r}_2 - \int\mu_{xc}[\rho_{in}]\rho_{in}d\mathbf{r} + E_{xc}[\rho_{in}]$$
$$+ \frac{1}{2}e^2\int\frac{\Delta\rho(\mathbf{r}_1)\Delta\rho(\mathbf{r}_2)}{|\mathbf{r}_1 - \mathbf{r}_2|}d\mathbf{r}_1 d\mathbf{r}_2 + \frac{1}{2}\int\frac{\delta^2 E_{xc}}{\delta\rho^2}\bigg|_{\rho_{in}}\Delta\rho(\mathbf{r}_1)\Delta\rho(\mathbf{r}_2)d\mathbf{r}_1 d\mathbf{r}_2 \tag{43}$$

The first line of equation 43 is known as the Harris-Foulkes functional [22]:

$$E_{\text{HF}} = \sum_{j \text{ occ.}}\epsilon_j - \frac{1}{2}e^2\int\frac{\rho_{in}(\mathbf{r}_1)\rho_{in}(\mathbf{r}_2)}{|\mathbf{r}_1 - \mathbf{r}_2|}d\mathbf{r}_1 d\mathbf{r}_2 - \int\mu_{xc}[\rho_{in}]\rho_{in}d\mathbf{r} + E_{xc}[\rho_{in}] \tag{44}$$

When self-consistency is reached (i. e. $\rho_0 = \rho_{in} = \rho_{out}$ with ρ_{in} the self-consistent density), this corresponds to the total energy; for this reason, if we were able to make a very good guess of ρ_{in}, then we would not need to perform the self-consistency cycle, and obtain the total energy to first order directly. Moreover, it can be shown (e.g. in [21]) that in the HF functional at ρ_0 the effective potential can be replaced by an arbitrary potential V_{eff} independent of the density; this implies that the potential could be calculated using a model that takes into account the non-locality of the exchange-correlation energy [21], eliminating the need for the LDA. Therefore better results could be obtained using the approximated HF functional rather than the exact full HKS functional.

Finally, including the contribution coming from the interaction between the nuclei, we can write 22 as

$$W(\mathbf{R}_I) = E[\rho_0] + \hat{V}_{nn} \tag{45}$$

It is instructive to take a closer look at this equation. Using 42, we can write a term U as the total electrostatic energy by including in addition to $V_{en}[\rho_0]$ and $C[\rho_0]$ the nucleus-nucleus interaction:

$$U = V_{en}[\rho_0] + C[\rho_0] + \hat{V}_{nn} \tag{46}$$

However, each of these terms, as defined by equations 21, 26 and 30, is divergent, as pointed out by Methfessel in [25]. In a system with periodic boundary conditions, this can be solved by rewriting U as

$$U = \int\rho_0(\mathbf{r}_1)V_{es}(\mathbf{r}_1)d\mathbf{r}_1 + \sum_I Z_I V_I$$

where V_{es} and V_I are the total electrostatic potentials felt by an electron and a nucleus:

$$V_{es}(\mathbf{r}) = e^2 \int \frac{\rho_0(\mathbf{r}_2)}{|\mathbf{r}_1 - \mathbf{r}_2|} d\mathbf{r}_2 - e^2 \sum_I \frac{Z_I}{|\mathbf{r}_1 - \mathbf{R}_I|}$$

$$V_I = e^2 \sum_{J \neq I} \frac{Z_J}{\mathbf{R}_I - \mathbf{R}_J|} - e^2 \int \frac{\rho_0(\mathbf{r}_1)}{|\mathbf{R}_I - \mathbf{r}_1|} d\mathbf{r}_1$$

U is now a sum over finite contributions from the unit cell [25].

In practice, calculating the energy involves choosing the basis set so that the guess of the density is optimised. Moreover, in crystals we impose boundary conditions and use Bloch's theorem to calculate $\epsilon_j(\mathbf{k})$ for a set of $\mathbf{k}$-vectors in the first Brillouin zone [22]. The density of states is then

$$n(\epsilon) = \sum_{j,\mathbf{k}} \delta(\epsilon - \epsilon_j(\mathbf{k}))$$

so that

$$\sum_{j \text{ occ.}} \epsilon_j = \int_{-\infty}^{\infty} f(\epsilon) \epsilon n(\epsilon) d\epsilon$$

where $f(\epsilon)$ is the Fermi function, which is 1 at 0 K, where the integral is evaluated up ϵ_F, the Fermi level.

3. METHODS

In this section we will give a brief overview of the computational methods that we used, as well as an account of the methodology followed in our research.

As was shown in the background theory section of this report, the stacking fault energies in the basal plane can be inferred from the energies of a number of perfect structures. The tool used to calculate these energies is DFT, which is implemented in the code we have used, i. e. *lmf*. lmf is part of the Questaal (Quasiparticle Electronic Structure and Augmented LMTOs) suite of electronic structure simulation programs [26], and it exploits the full potential Linear Muffin Tin Orbital (FP-LMTO) method based on smooth Hankel functions (i.e. a convolution of a Hankel and Gaussian function [26]: their mathematical properties can be found in [27]), described by M. Methfessel et al. in [28]. The main feature of this method is that space is partitioned into atom-centered muffin-tin spheres and an interstitial region, so that the potential integrals are divided into the contributions coming from the two types of region [28]. The integrals over the muffin-tin spheres are calculated by expressing the potential and the basis functions in polar coordinates around the sphere centre in terms of the radius and spherical harmonics [28] and solving the radial Schrödinger equation, obtaining *partial waves* [26]. In order to solve the integrals over the interstitial regions, the interstitial potential and density are specified at each point of a real-space mesh, while the envelope functions of the interstitial are chosen to be smooth Hankel functions, which "bend over" as they approach the centre of the atomic sphere so that the connection between the interstitial region and the sphere is smooth. The Hankel functions are then "augmented" (i.e. replaced) with the solutions to the radial Schrödinger equation (the *partial waves*) inside the sphere.

It should be noted that the choice of basis functions is one of the most sensitive steps in DFT calculations; as such, over the years several methods have been devised, and the FP-LMTO method, although very successful, is not the only one. Alternatively, the smooth envelope functions can be chosen to be plane waves; this is the case for the linear augmented plane-wave (LAPW) method, described by Andersen in [29]. Moreover, smooth Hankel functions and plane waves can be combined in what is called a planar muffin tin (PMT) basis set, as discussed by Kotani and van Schilfgaarde in [30].

In the FP-LMTO method, the charge density is then made up of three parts: a smooth density n_0 carried on a uniform mesh, defined everywhere in space; the true density n_1 expressed in terms of spherical harmonics inside each augmentation sphere; and a one-center expansion n_2 of the smooth density that appears in the spherical harmonics, inside the sphere, so that the total density is $n = n_0 + n_1 - n_2$ [26]. This input density is then used to solve the Poisson equation, which yields the electrostatic potential, added to the exchange-correlation potential to obtain the full potential [28]. As mentioned in the background theory section, the xc-potential is calculated using the LDA. This is the somewhat crudest approximation one could make, and it is not accurate when the density varies rapidly. A more precise approach takes into account the gradient of the density in what is called the generalised gradient approximation (GGA), explained in [31]; in our calculations we therefore use the GGA with the PBE (Perdew-Burke-Ernzerhof) functional for rapidly varying density. The KS equations are then solved using the full potential, and the density obtained from the output is used as the new input density for the following iteration, until self-consistency is reached.

The various tasks in the calculation are carried out by the executables of the full potential suite. The input density is generated by lmfa, which writes it in a file atm.ext. lmfa also generates the parameters for the basis set, and writes them in a basp0 file. The augmentation sphere overlap is checked by the executable lmchk, which can also calculate automatically the sphere radius. Finally, lmf uses the input density to carry out the self-consistent calculation.

The input system is unique for this suite of codes; the main input file (the ctrl file) is used to define the initial parameters. Here we specify the parameters for the crystal structure (the lattice vectors, atom species and positions, augmentation sphere radii for each species), for the hamiltonian (the energy cutoff for the plane wave mesh, the exchange and correlation functional, the basis set), for the Brillouin zone integration (k-mesh, integration method), and for iteration cycle (number of iterations, convergence criteria).

In the earliest stages of our research, we conducted a series of test calculations in order to probe the behaviour of the total energy as a function of some parameters, namely the number of k-points, the G-vector cut-off GMAX, the convergence criteria CONV and CONVC, and the Brillouin zone integration method. All the tests were conducted on a two-atom unit cell of hcp magnesium.

Once the parameters were optimised, we calculated the energies of the five perfect structures with ideal axial ratio, maintaining the volume per atom fixed in each structure (155.3163 au^3), using a $30 \times 30 \times 30$ k-mesh and tetrahedron integration of the Brillouin zone. We used a two-atom cell for 2H, a one-atom cell for 3C, a four-atom cell for 4H, a six-atom cell for 6H and a nine-atom cell for 9R. For two structures (4H and 6H) the energies were calculated using two different ctrl files to check for consistency: in one of the files, the lattice vectors and the atomic positions were entered manually,

whereas in the other one they were obtained from cif files for Samarium (4H) and the 6H polytype of silicon carbide. Interactions between neighbours were then calculated up to J_4, in order to establish how quickly the interaction decays as further neighbours are included. The stacking fault energies for pure Mg were then calculated for each number of neighbours included. For the cases of neighbours up to J_1, up to J_2 and up to J_3, we were able to calculate the interaction coefficients and the stacking fault energies using several combinations of structures (defined in the results section of this report), which allowed us to check the consistency of our results.

In order to conduct further checks on our results, we then calculated the SFE for the fault I_2 for Mg with ideal axial ratio using the supercell method described by Andritsos et al. in [32]. This method will not be discussed in detail in this report; it involves creating a supercell using the lmscell executable (part of the LMTO package), and then modifying it in order to obtain a structure containing a stacking fault, using homogeneous shear boundary conditions. The energy of the supercell is calculated, and then compared to the energy of the perfect crystal to obtain the SFE, as described by Chou et al. in [33]. We created a 24 atom supercell by elongating the two-atom hcp unit cell in the z-direction. We reduced the K-mesh to $30 \times 30 \times 20$ points; this was done to improve convergence, and is justified by the size of the cell, which is long enough for less detail to be needed in the k-mesh. Atomic relaxation was allowed along the direction perpendicular to the plane of shear, i.e. along the z-axis; this allows the atoms to move in order to minimise the forces created by the presence of the stacking fault. To this end, we added a token DYN in the ctrl file, which defines how relaxation is performed and its convergence criteria.

Once the full analysis on pure Mg had been conducted, we focused our attention on Mg alloys. We studied binary alloys of Mg-Li, Mg-Ca and Mg-Zn at 1.56% atomic alloy concentration as well as Mg-Ca at 0.78% atomic concentration, using 64 and 128 atom supercells. We truncated the series at first nearest neighbour, hence calculating the energies of the fcc and hcp structures only. For both structures, a $20 \times 20 \times 20$ k-mesh was used. Relaxation was performed in all directions, in order to allow the atoms to give in to the forces created by the presence of the alloying element. Since conducting relaxation makes the calculations more computationally demanding, for the case of the alloys we performed the non-self-consistent calculation using the Harris-Foulkes functional.

4. RESULTS AND ANALYSIS

In the following section, the results we obtained are reported, and an analysis of these is conducted.

I. Test calculations

The first atomistic simulations that were carried out were test calculations on a two-atom cell of pure hcp Mg with axial ratio 1.627, applying periodic boundary conditions. The first parameter that we tested was the number of k-points, which is a product of the number of divisions for the three directions of the reciprocal lattice vectors [26]. This is not, however, the irreducible number of

k-points, which is found after symmetry operations are applied. The results of the calculations are presented in figure 5.
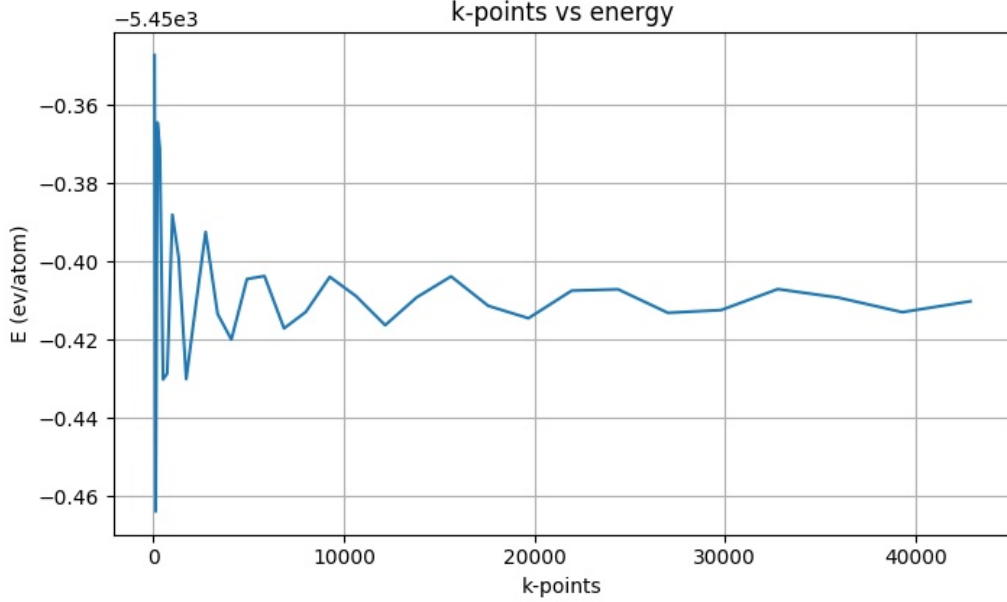

FIG. 5. This graph shows a plot of the number of k-points versus the energy. As the number of k-points is increased, the energy converges toward a mean value.

It can be seen that the energy presents an oscillatory behaviour as the number of k-points is increased, then converging towards a mean value as the k-mesh becomes more detailed. We find the amplitude of the oscillation to become relatively small at around 25000 k-points, within a range of ~3 meV; therefore we take 27000 k-points (corresponding to a 30×30×30 k-mesh) to have a sufficient level of accuracy, and use it henceforth in all our calculations of the energies of the perfect structures. Subsequently, we tested two different methods for the integration of the Brillouin zone. The calculations for the k-mesh described above were carried out using the Methfessel-Paxton sampling method [34], which is an extension of the Gaussian-broadened sampling integration method. Having fixed the k-mesh, we tried implementing the tetrahedron integration method instead [35]. As far as testing in the literature goes ([36]), tetrahedron integration is reported to have more accurate results; however, the Gaussian integration method is known to greatly improve convergence. We found that the energy calculated using tetrahedron integration and a 30×30×30 k-mesh is closer to the mean of the oscillation, hence more precise. As a consequence, we resolved to using tetrahedron integration for our calculations, at least in the case of the perfect structures, since the cells we used contained only few atoms and we did not expect them to have any convergence issues. However, when running simulations of bigger supercells containing stacking faults or alloys, we had to reconsider the use of the Methfessel-Paxton integration method, as convergence issues arose.

Another parameter to be tested was the G-vector cutoff GMAX. This is the plane-wave cutoff used to represent the density in reciprocal space, and it is determined by the breadth of the peaks of the envelope functions [26]. The minimum value for this parameter is estimated by lmfa; for our two-atom

cell, lmfa prints the value of 5.1 Ry$^{\frac{1}{2}}$. We tested the behaviour of the energy for a range of GMAX between 3 and 10 Ry$^{\frac{1}{2}}$.
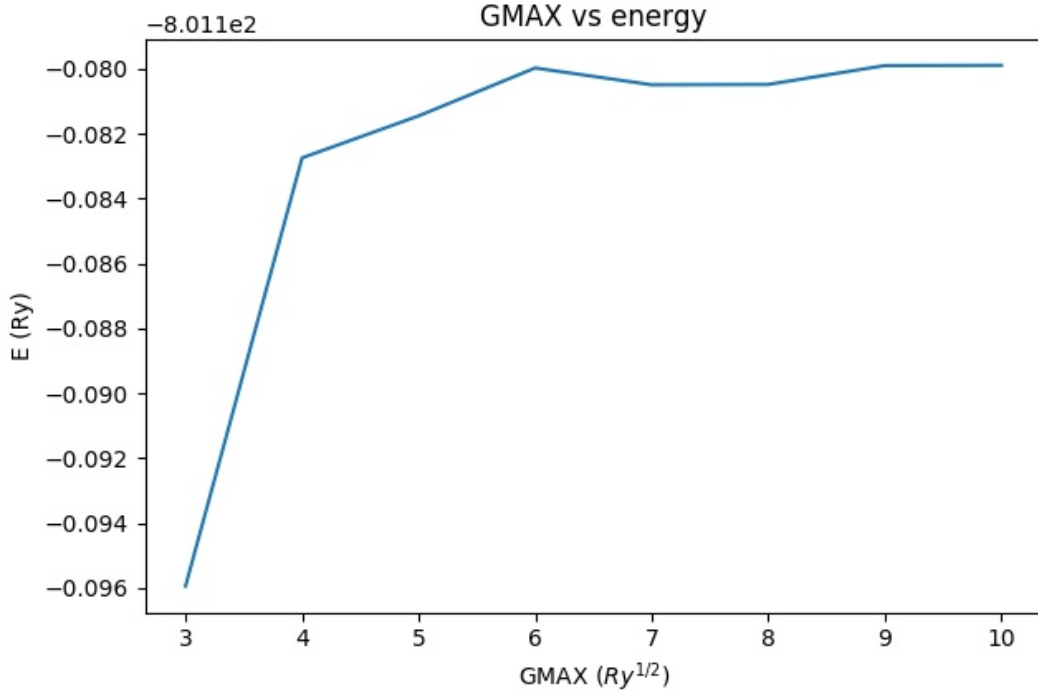
FIG. 6. This graph is a plot of GMAX (i.e. the plane wave cutoff) versus the energy. It can be seen that the energy stabilises as GMAX is increased.

As seen from the graph in figure 6, the energy increase sharply between 3 and 4 Ry$^{\frac{1}{2}}$, and stabilises around the range of 6 to 8 Ry$^{\frac{1}{2}}$. Therefore the value estimated by lmfa seems a reasonable choice, and one we decided to stick to for the following calculations; however, increasing GMAX will be necessary in order to improve the convergence in the case of supercells.

Finally, we conducted tests on the convergence criteria. CONV defines the maximum energy change from the prior iteration for self-consistency to be reached [26]; CONVC defines the self-consistency criteria for the electron density.

21

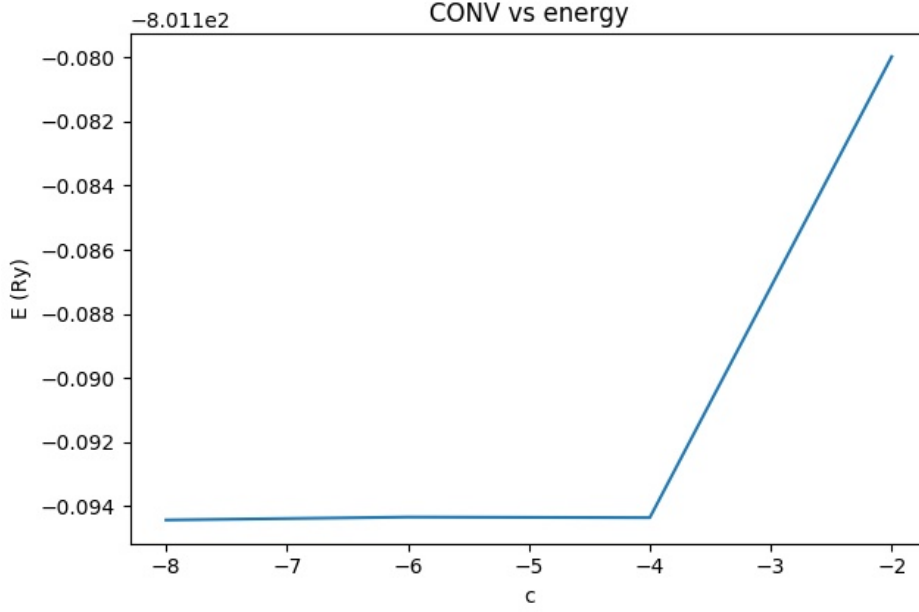FIG. 7. This graph is a plot of CONV (i.e. the maximum energy difference between two iterations accepted for convergence) versus the energy. Here c represents the exponent of CONV, i.e. $\text{CONV} = 10^c$ Ry. It can be seen that the energy is self-consistent for CONV around 10^{-4} Ry.
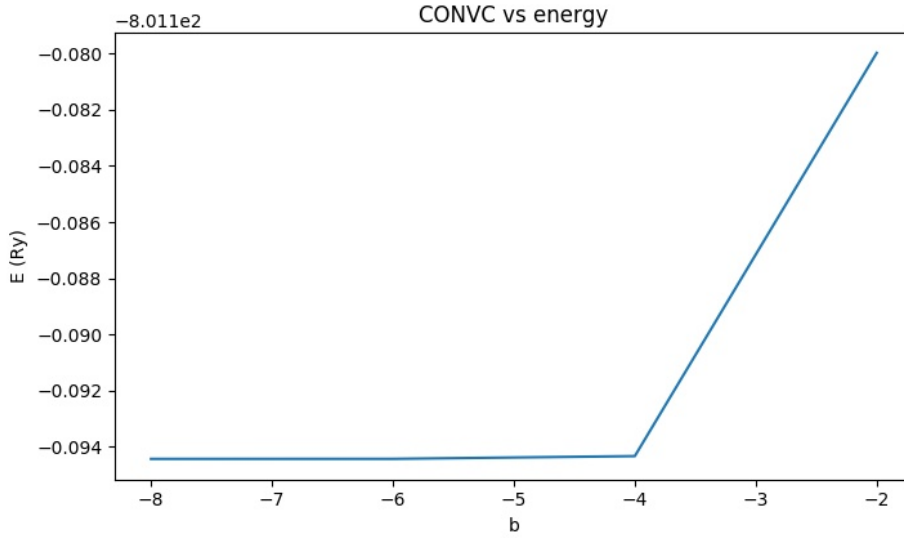
FIG. 8. This graph is a plot of CONVC (i.e. the maximum density difference between two iterations accepted for convergence) versus the energy. Here b represents the exponent of CONVC, i.e. $\text{CONVC} = 10^b \; \frac{e}{bohr^3}$. It can be seen that the energy is self-consistent for CONVC around $10^{-4} \; \frac{e}{bohr^3}$.

In both cases, as shown in figures 7 and 8, the energy is minimised when convergence criteria are set to 10^{-4}. This means that the tolerance is small enough to reach self-consistency. In order to be even more precise, we adopted $\text{CONV} = \text{CONVC} = 10^{-6}$ for the calculations of the energies of the perfect structures.

II.   J-parameters and SFEs for pure Mg

Once the parameters of the input file were optimised, we proceeded to the calculation of the energies of the perfect crystals, using the ideal axial ratio. We used a $30\times30\times30$ k-mesh for the Brillouin zone and integrated using tetrahedron integration; the self-consistent calculation was performed with convergence criteria $CONV = CONVC = 10^{-6}$. Maintaining the volume of the unit cell constant, for the hexagonal structures and the 9R structure we used a lattice constant $a_h = 6.0336$ au (3.1928 Å), while for the cubic structure we used $a_c = 8.5328$ au (4.5154 Å). The augmentation sphere radius and the basis set were calculated using lmchk and lmfa for the 3C structure; the same radius and basis set were then used for the other structures. The following table reports the energies of the structures in relation to the 2H structure, given in eV/atom and kJ/mol.

s. c. E \ s	2H	3C	4H	6H	9R
eV/atom	-5451.3823	$+0.0131$	$+0.0059$	$+0.0086$	$+0.0029$
kJ/mol	-525978.67	$+1.27$	$+0.57$	$+0.84$	$+0.28$

TABLE I. This table shows the energies of the polytypes (labelled by s) of pure Mg with ideal c/a., calculated by lmf via the self-consistent (s. c.) cycle. The energy of the 2H structure is given both in ev/atom and kJ/mol, and the energies of the other structures are relative to that of 2H, i.e. as differences in energy.

The energy of the 2H structure is the lowest, as is expected of Mg, whereas the energy of 3C is the highest one. At this point it is worth discussing error and its sources on the values we obtained for these energies. The main sources of error in the DFT calculation would be the LDA and the GGA (which we used), which are both approximations. However, the GGA is known to give good results, in good agreement with experimental measurements; the error linked with it is therefore regarded as controlled. For a review on error due to the GGA, refer to [37]. Other possible sources of error include the choice of basis set and the accuracy of the k-mesh. Concerning the basis set, this has been the focus of attention over the past few years, and we will regard as optimised its estimate done by lmfa. The k-point mesh is known to affect the energy, as indeed we have studied in the previous section; however, having conducted our test calculations, we consider this optimised to the desired level of accuracy.

Once the energies of the polytypes were obtained, we created twenty-six combinations of structures, assigning to each of them a letter of the latin alphabet. Combinations A-J are made of two polytypes each, and hence exploit the $AN(N)^1I$ model that includes only nearest neighbours and coefficients up to J_1. Combinations K-T are made of three polytypes, and are used in the $AN(N)^2I$ model, with coefficients included up to J_2. Combinations U-Y are made of four structures, so that J-parameters up to J_3 can be calculated for the $AN(N)^3I$ model. Finally, combination Z contains all five structures and allows us to calculate all parameters up to J_4, i.e. the coefficients of the $AN(N)^4I$ model.

N	combination (t)	2H	3C	4H	6H	9R
1	A	X	X			
	B	X		X		
	C	X			X	
	D	X				X
	E		X	X		
	F		X		X	
	G		X			X
	H			X	X	
	I			X		X
	J				X	X
2	K	X	X	X		
	L	X		X	X	
	M	X		X		X
	N	X			X	X
	O		X	X	X	
	P		X		X	X
	Q			X	X	X
	R	X	X			X
	S	X	X		X	
	T		X	X		X
3	U	X	X	X	X	
	V	X		X	X	X
	W	X	X	X		X
	X		X	X	X	X
	Y	X	X		X	X
4	Z	X	X	X	X	X

TABLE II. In this table the possible combinations of polytypes are defined. Here n refers to the number of neighbours included, so that the AN(N)^{N}I model is used. E. g., for N=1 only the first neighbour is included, and two structures are sufficient to calculate coefficients up to J_1. A letter of the latin alphabet is assigned to each combination of polytypes.

Subsequently, for each combination of polytypes the relevant J-coefficients were calculated. This was done by truncating the series 2 to 6 at the desired number of neighbours, and then reworking the equations of the chosen structures to obtain expressions for the J's. The energies obtained using DFT were then inserted in the equations and the J-parameters were calculated in units of meV/atom, as presented in the following table.

N	1										2	
t \\ J_n	A	B	C	D	E	F	G	H	I	J	K	L
J_1	−6.6	−5.9	−6.5	−4.3	−7.3	−6.7	−7.7	−8.3	−9.0	−8.6	−6.6	−7.1
J_2	-	-	-	-	-	-	-	-	-	-	−0.3	−0.6
J_3	-	-	-	-	-	-	-	-	-	-	-	-
J_4	-	-	-	-	-	-	-	-	-	-	-	-

N	2						3				4	
t \\ J_n	N	P	Q	R	S	T	U	V	W	X	Y	Z
J_1	−8.6	−8.6	−8.6	−6.6	−6.6	−8.1	−6.8	−6.3	−7.3	−7.9	−7.1	−7.1
J_2	−2.1	0.9	0.2	−1.1	−0.1	0.4	−0.3	0.2	−0.3	0.2	−0.6	−0.3
J_3	-	-	-	-	-	-	0.3	0.8	0.8	0.3	0.5	0.5
J_4	-	-	-	-	-	-	-	-	-	-	-	−0.2

TABLE III. This table shows the results obtained for the J parameters for each combination of structures, given in meV/atom. It should be noted that the capital N refers to the model used, whereas n refers to the interaction coefficient.

The results tend to vary quite significantly. The values obtained for J_1 are always negative, and average to −7.3 meV, with peaks at −4.3 and −9.0 meV for combinations D and J respectively; It can be noted that both these combinations contain the 9R structure. While we do not have error bars coming from the DFT calculation of the energies, we can estimate an error coming from our Ising-like description. The uncertainty on our set of J_1's can be calculated from the spread of the data as follows:

$$\Delta J_1 = \frac{J_{1max} - J_{1min}}{2}$$

The uncertainty on the average is then

$$\Delta \bar{J}_1 = \frac{\Delta J_1}{\sqrt{N}} \tag{47}$$

where N is the number of values obtained for J_1. Applying this to the data in our table we obtain $\Delta \bar{J}_1 = 0.5$ meV, so that the average is $\bar{J}_1 = -7.3 \pm 0.5$ meV.

As expected from the Ising-like model we have used, the values obtained for J_2 are always smaller in magnitude than the values of J_1; however in this case the signs are not always in agreement, with nine combinations yielding negative results and the remaining four giving positive results. The peaks here are more significant, and the fluctuations are larger than in the case of J_1. We can calculate the average and the error on the average in this case as well; using equation 47, we find $\bar{J}_2 = -0.3 \pm 0.4$ meV. This is a large error, which reflects the fluctuations in the data.

The values obtained for J_3 are instead all positive, and only for one combination out of six they are smaller in magnitude than J_2; their fluctuation is however less significant. Using again 47, we find the average to be $\bar{J}_3 = 0.5 \pm 0.1$ meV. Finally, the one value obtained for J_4 from combination Z is positive and smaller in magnitude than both J_2 and J_3.

Looking at the table as a whole, we can see that combination Z, which includes the largest number of neighbours, gives the results that best fit the averages. Moreover, while the hierarchy of the J-parameters does not always follow the predicted one (as is the case for J_2 being often smaller than J_3), it should be noted that in nearly the totality of the cases J_1 is at least one order of magnitude greater than the other coefficients. This can be seen graphically in figure 9. In addition, we would like to stress the scale of the problem: the J-coefficients that we have calculated are due to very small differences in the energies of the perfect structures; this makes them very small in comparison to J_0, which is of the order of the energy of the 2H structure. Thus the contribution to the total ground state energy of the crystal coming from the interactions between neighbouring layers is a very small one. In this context, the error on our data is a reflection of the scale of the theory, and this translates into the stacking fault energy being very small.
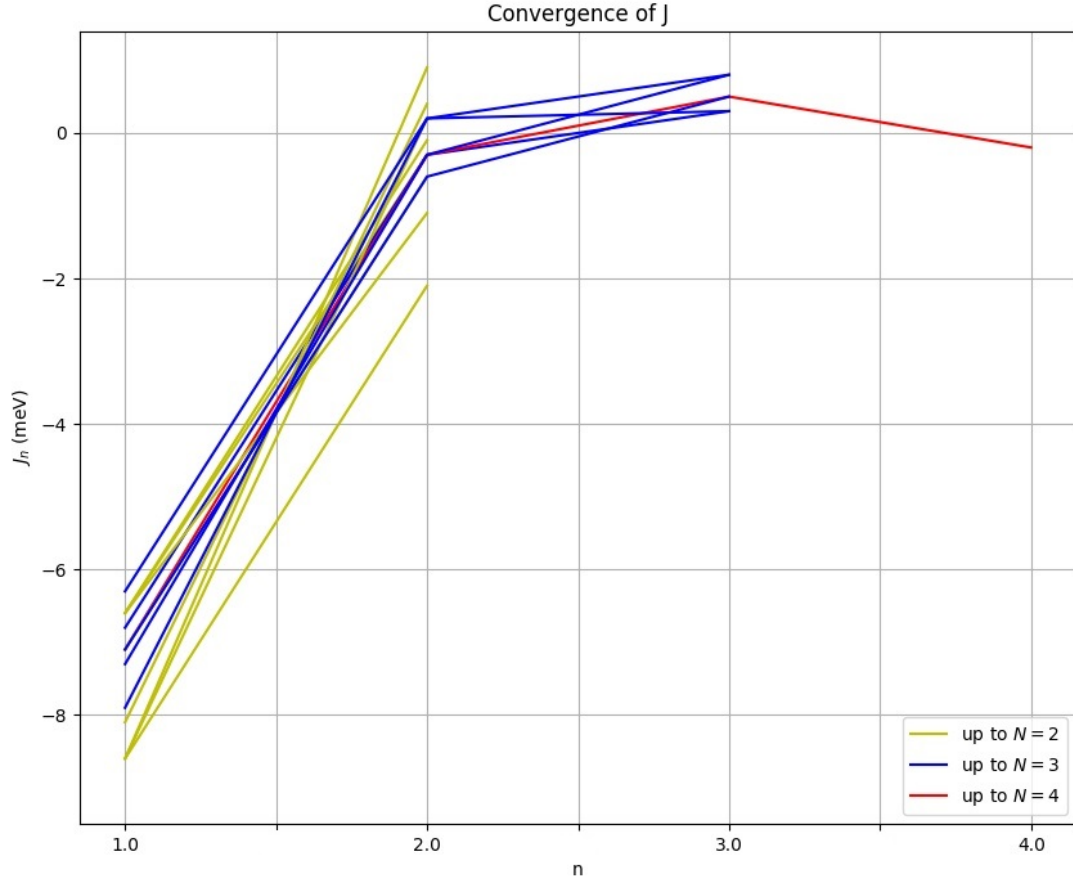

FIG. 9. This graph is a plot of J_n against n, i.e. the number of neighbours. The yellow lines mark the trends followed by combinations K to T, in which neighbours up to J_2 are evaluated; the blue lines refer to combinations U to Y, which include up to J_3, and the red line reports the trend of combination Z, with neighbours up to J_4.

Comparing our results with the literature, Hu and Yang in [18] found $J_1 = -8.6$, $J_2 = -1.3$ and $J_3 = -0.7$ meV, for calculations performed using the local spin density approximation (LSDA) and

$J_1 = -8.2$, $J_2 = -1.3$, $J_3 = -0.7$ meV using the GGA with PBE functional. However, they used axial ratios 1.599 (LSDA) and 1.600 (GGA), which are not only far from ideal, but also from the experimentally calculated ratio, i.e. 1.623 [18]. Therefore, it is not very sensible for us to compare our results with theirs quantitatively, but we should rather compare them qualitatively; in this sense, the results are in good agreement, being of the same order of magnitude if not always having the same sign.

It can be seen that in table III the J-coefficients for combinations M and O are not listed. The reason for this is that for these combinations, once we truncate the series for the energies at J_2 and rework the equations, we find that the J's cancel and we are left with a single equation connecting the energies of the three structures, meaning that up to J_2 these energies are linearly dependent on each other. For combination M we find $3E_{9R} - 2E_{4H} - E_{2H} = 0$, while for O we have $3E_{6H} - 2E_{4H} - E_{3C} = 0$. Therefore one of the three energies can be obtained from the other two; this allows us to test the ANNNI model further, by comparing the energy calculated in this way to that obtained using DFT, as shown in table IV.

t ⟍ s ⟍ E	M			O		
	2H	4H	9R	3C	4H	6H
E_{ANNNI}	-0.0131	$+0.0043$	$+0.0039$	$+0.0142$	$+0.0064$	$+0.0083$
E_{DFT}	0.0	$+0.0059$	$+0.0029$	$+0.0131$	$+0.0059$	$+0.0086$
Diff	30.8×10^{-4}	15.4×10^{-4}	10.3×10^{-4}	10.4×10^{-4}	5.2×10^{-4}	3.5×10^{-4}

TABLE IV. Combinations M and O, which have n=2, present a degeneracy in energy, meaning that the energy of one of the polytypes can be obtained from the energy of the other two. For M, $3E_{9R} - 2E_{4H} - E_{2H} = 0$; for O, $3E_{6H} - 2E_{4H} - E_{3C} = 0$. This table shows how the energies calculated via the ANNNI model compare with the energies calculated by lmf using self-consistent DFT. Energies are given in units of ev/atom.

It can be seen that combination O presents better agreement between the two energies than combination M; although the differences in both cases seem small, they are not negligible if we remind ourselves of the scale of the problem, mentioned earlier, such that our calculations of the J parameters are in fact based on very small differences in energies.

N	1										2	
t $\diagdown$ γ	A	B	C	D	E	F	G	H	I	J	K	L
γ_{I_1}	23.9	21.4	23.6	15.8	26.4	24.5	27.9	30.2	32.6	31.4	21.4	21.4
γ_{I_2}	47.8	42.8	47.2	31.6	52.8	49.0	55.9	60.3	65.2	62.8	45.3	47.1
γ_E	71.7	64.2	70.8	47.4	79.2	73.5	83.8	90.5	97.8	94.1	69.2	72.8
γ_{T_2}	47.8	42.8	47.2	31.6	52.8	49.0	55.9	60.3	65.2	62.8	42.8	42.7

N	2						3				4	
t $\diagdown$ γ	N	P	Q	R	S	T	U	V	W	X	Y	Z
γ_{I_1}	15.8	38.2	32.5	15.8	23.2	32.5	19.5	15.8	15.8	26.9	15.8	13.9
γ_{I_2}	47.1	69.5	63.9	39.6	47.1	45.3	62.0	41.6	45.3	56.4	43.4	43.4
γ_E	78.4	100.9	95.2	63.5	70.9	91.4	69.2	61.8	69.2	84.0	67.3	65.5
γ_{T_2}	31.5	76.4	65.1	31.5	46.5	65.1	40.9	37.2	37.2	55.7	35.3	35.3

TABLE V. This table presents the results obtained for the energies of the four types of stacking faults calculated via the $AN(N)^NI$ model using various combinations of polytypes. The SFEs are calculated in terms of energy per unit area (γ) and given in units of mJ/m^2.

Once the J-parameters were obtained, equations 12 to 15 were used, together with 16, to obtain the stacking fault energies per unit area. The results are given in table V in units of mJ/m^2, as per the literature.

First of all, we shall look at the hierarchy of the energies of different types of stacking faults. The energy of the extrinsic stacking fault E is the highest one, whereas the lowest is that of I_1. This could already be predicted by looking at equations 12 to 15, and is in agreement with the literature [3, 5, 18, 38–40]. However, in the literature, in which the supercell method is used, T_2 is found to have higher energy than I_2; in our data, to first order in J they are the same, whereas to higher order γ_{T_2} is often lower than γ_{I_2}. This finds confirmation in the paper by Hu at al. [18] quoted above, who use the ANNNI model; in fact, they found $\gamma_{I_1} = 0.03$ J/m^2, $\gamma_{I_2} = 0.06$ J /m^2, $\gamma_E = 0.09$ J/m^2, $\gamma_{T_2} = 0.06$ J/m^2 (using the LSDA) and $\gamma_{I_1} = 0.03$ J/m^2, $\gamma_{I_2} = 0.06$ J/m^2, $\gamma_E = 0.09$ J/m^2, $\gamma_{T_2} = 0.05$ J/m^2. For this reason, this might be interpreted as a feature of an Ising-like description if far enough neighbours are taken into account. Since the magnitude of the energy of the stacking fault determines its stability [18], it can be predicted that the occurrence of I_1 should be more likely than that of E; generally, the two stacking faults more likely to occur should be I_1 and I_2, which are also the most stable. It could be argued that the energy of T_2 is roughly of the same order of that of I_2 (in our case even smaller for some combinations), meaning that it should be nearly just as likely for a T_2 fault to occur. However, this is not the case, and in fact the T_2 stacking fault has not been reportedly observed in Mg yet, according to Wen et al. [38]; the reason they provide for this resides in the unstable SFE (which we have only briefly touched upon in the theory section of this report, and have not calculated in any way), which is much larger for T_2 than it is for I_2. This constitutes a barrier for the formation of T_2, which is thus less likely to occur. In addition, as is pointed out by Chetty and Weinert in [5], a T_2 fault is likely to decay into two I_1 faults, which have lower energies, and an E fault should decay into

I_1 and I_2 faults. This said, the concentration and distribution of different types of stacking faults are not only a consequence of their energies, but also of other factors such as entropy. Therefore, while energy considerations can help predict the occurrence of the faults, they do not constitute the whole picture.

Secondly an estimate of the errors on the SFEs can be given through error propagation, i.e. by observing how the error on the average of the J-parameters propagates through the calculations. The formula for error propagation for γ_{I_1} derived using equations 12 and 16 is the following:

$$\Delta\gamma_{I_1} = \frac{\sqrt{(2\Delta\bar{J}_1)^2 + (4\Delta\bar{J}_2)^2 + (4\Delta\bar{J}_3)^2}}{A} \tag{48}$$

Similar equations can be derived for γ_{I_2}, γ_E and γ_{T_2}, so that the uncertainties are found to be $\Delta\gamma_{I_1} = 3.6$ mJ/m^2, $\Delta\gamma_{I_2} = 4.7$ mJ/m^2, $\Delta\gamma_E = 6.3$ mJ/m^2 and $\Delta\gamma_{T_2} = 7.0$ mJ/m^2. Since they contain errors coming from the averages of all the J-parameters that we have calculated, they can be taken to be the uncertainties on the SFEs obtained for combination Z, whose J-parameters were also the closest ones to the averages. The main contributions to the magnitude of the error bars come from the uncertainties on J_1 and J_2; in particular, a great source of uncertainty comes from J_2, whose error bar is large especially compared to its magnitude. This is the reason for the error bar on γ_{T_2} being larger than that of γ_E.

Another point that should be noted from this table is that there is a generalised convergence issue. All the SFEs oscillate for different combinations, and this is due mainly to the fluctuations in J_1 and the large discrepancies between different values of J_2 (including the signs not always in agreement). The only SFE that seems to converge as more neighbours are taken into account is that of I_2; the SFE of I_1 oscillates and then becomes smaller as N increases, and so do the energies of E and T_2. This is due to J_2, J_3 and J_4 being all of the same order of magnitude; although the magnitude of the J coefficients decreases steeply after J_1, it does not decay to very small values fast enough for the SFE to converge. On the other hand, it can be seen that the SFE depends mainly on J_1; this is more evident for I_2.

Subsequently, we shall compare our results to the literature. All the results we are going to present were calculated using the supercell method and DFT axial ratio; for this reason our comparison will be mainly qualitative. Among the literature, Smith [39] and Chetty and Weinert [5] have used the plane wave pseudopotential method, obtaining for the energy of I_1 18 [39] (using the GGA with the PBE functional) and 21 [5] (using the LDA) mJ/m^2; $\gamma_{I_2} = 36$ [39], 44 [5] mJ/m^2, $\gamma_E = 58$ [39], 69 [5] mJ/m^2, $\gamma_{T_2} = 40$ [39], 51 [5] mJ/m^2. The projector augmented wave (PAW) method [41] along with the GGA with the PW91 functional [42] were used by Wen et al. [38] and Wu et al. [43], whereas Yin et al. [40] and Sandlöbes et al. [44] used the PBE functional; they obtained $\gamma_{I_1} = 16$ [38], 21 [43], 18 [40], 20 ±1 [44] mJ/m^2, $\gamma_{I_2} = 34$ [38], 34 [40] mJ/m^2, $\gamma_E = 59$ [38], 54 [40] mJ/m^2, $\gamma_{T_2} = 38$ [38] mJ/m^2. Finally, Andritsos et al. [32] used the same FP-LMTO method that we used, along with the GGA with the PBE functional, and found for the SFE of I_2 32.1 mJ/m^2. It can be noted that these results are in good agreement with each other, especially in the case of the I_2 fault. Comparing with our results, it can be seen that for most combinations the SFEs for I_1 and T_2 were found to be lower than those calculated in the literature, whereas that of I_2 is nearly always higher, and the same can

be said for the fault E. These discrepancies could be due to the difference in the axial ratio; however further studies are needed to establish this with surety.

In addition, in order to establish a direct comparison with the supercell method, we calculated the SFE for I_2 following the steps described by Andritsos et al. in [32], using the ideal axial ratio. In order to do so, we used a two-atom hcp cell to create a $1 \times 1 \times 12$ 24-atom supercell. We used homogeneous shear boundary conditions to modify the cell such that it contained an I_2 fault, and consequently we calculated the self consistent energies of the perfect crystal and of the faulted structure, using a $30 \times 30 \times 20$ k-mesh, the Methfessel-Paxton sampling integration and allowing the atoms to relax along the z-axis (in the case of the structure containing the stacking fault). Calculating the SFE as the difference in energy between the two structures, we found $\gamma_{I_2} = 44.5$ mJ/m^2. Now it should be noted that in the AN(N)^{N}I model the energies are calculated from unrelaxed structures, as the model is based on the assumption that the distance between layers remains constant. In allowing relaxation along the z-axis, we allow the distance between layers to change; therefore to have an accurate comparison with our result we should use the energy calculated for the unrelaxed supercell containing the stacking fault. However, we have found that due to the ideal axial ratio, the forces on the atoms remain insignificant even when the stacking fault is added, and therefore the self consistent energy is the same before and after relaxation is performed. The result we obtained is then in good agreement with the energies calculated using 14 out of 24 combinations with the AN(N)^{N}I model, and in particular with combination Z. However, it should be noted that the supercell method is heavily affected by a number of factors, as pointed out by Andritsos et al. [32] and Wang et al. [45], namely the size of the supercell, the k-mesh and the basis set. Having not tested out these factors in our work, we acknowledge that results may vary according to these parameters.

III.   Mg alloys

Having tested the AN(N)^{N}I model on pure magnesium with ideal axial ratio, we focused our attention on certain binary Mg-alloys, namely Mg-Li, Mg-Ca and Mg-Zn, always keeping the axial ratio ideal. We concentrated our work on diluted alloys, creating supercells and positioning alloying elements in the bulk, assuming that they would not be in proximity of the stacking fault; this assumption is necessary seen as the model does not allow the fault to be localised, as the SFE is calculated indirectly from the energy of perfect structures. Having established the main dependence of the SFE (in particular that of the fault I_2) on nearest neighbour interactions, we used two 64-atom supercells of fcc and hcp magnesium to calculate J_1. We investigated Mg-1.56at%Li, Mg-1.56at%Ca and Mg-1.56at%Zn; in addition, we calculated the SFEs for Mg-0.78at%Ca, since calcium reportedly has limited solubility in magnesium [46]. We employed a $20 \times 20 \times 20$ k-mesh and the Methfessel-Paxton sampling integration, and performed relaxation in all directions in order to allow the atoms to move according to the forces created by the presence of the alloying elements. We performed the non-self-consistent (nSC) calculation of the energy using the Harris-Foulkes (HF) functional [47] [48]. This was done in order to reduce significantly the computational time needed to perform the relaxation of a large supercell, taking into account that the efficiency of the nSC calculation has been

demonstrated not to come at the cost of accuracy; in fact, the HF functional is known to produce precise results, sometimes with even better accuracy than the SC calculation performed with the Hohenberg-Kohn functional. The HF functional has been tested extensively and compared to the HK functional a number of times in the literature, for example in [49–51].

γ \ alloy	Mg-1.56at%Li	Mg-1.56at%Ca	Mg-1.56at%Zn	Mg-0.78at%Ca
γ_{I_1}	24.2	27.7	22.2	26.8
γ_{I_2}	48.4	55.4	44.4	53.6
γ_E	72.5	83.1	66.7	80.3
γ_{T_2}	48.4	55.4	44.4	53.6

TABLE VI. This table presents the results obtained for the energies of the four types of stacking faults in Mg alloys calculated via the ANNI model. The SFEs are calculated as energies per unit area (γ) and given in units of mJ/m^2.

In the literature, ref [52] reported that a low concentration of zinc should leave the SFE essentially unchanged, while the addition of lithium to magnesium should increase the SFE, for $\sim 2\%$ concentrations; ref [53] presented similar conclusions, reporting however only a very small increase in the case of the addition of lithium, for low concentrations. In ref [54], the addition of zinc at $\sim 1\%$ concentration reportedly resulted in a small increase of the SFE for I_1 and I_2. Overall, as observed by Andritsos et al. [32], low concentrations of Li and Zn in Mg should not affect the SFE greatly, as evidenced by the results in [55] for γ_{I_2} with axial ratio 1.627, i.e. 36.6 mJ/m^2 for Mg-1.56at%Li and 31.5 mJ/m^2 for Mg-1.56at%Zn (pure Mg $\gamma_{I_2} = 32.1$ mJ/m^2) . If we take the SFEs calculated for combination A as the reference energies for pure Mg, we observe that in our case the addition of Li causes essentially no change in the SFE, while the addition of Zn slightly decreases it.
Concerning Mg-Ca diluted alloys, the literature predicts a decrease in the stacking fault energy with respect to pure Mg; this is the case for refs [53], [56] ($\sim 1\%$ concentration) and [57] (0.78% and 0.69% concentrations). From our data we report instead a significant increase in the SFE for both concentrations, in agreement with the result obtained by Andritsos [55] for Mg-0.78at%Ca, i.e. 40.3 mJ/m^2 for I_2.

5. FURTHER WORK AND CONCLUSIONS

In the theory section of this report, we described four types of stacking faults in the basal plane and presented the AN(N)^{n}I model used to calculate their energies, as well as giving an introduction to DFT. We then gave an account of the methodology followed throughout our research and of the computational methods we used; we presented the results we obtained for the J-parameters of the theory and the SFEs of pure magnesium with ideal axial ratio, as well as those of a number of binary Mg alloys.
The completion of this project leaves a number of questions unanswered. First of all, an object for further discussion is the discrepancies found among the J_1 and J_2 parameters calculated using various

polytype combinations for pure Mg, which result in largely varying results for the SFEs. In addition, although a main dependence of the SFE on J_1 was found, one may still ask if the interaction energies decay fast enough to justify the use of the ANNI model. While the comparison offered by the literature presents encouraging results, we suggest that in the future the energy of another structure may be calculated in order to obtain more data and possibly find a sharper trend.

Moreover, in order to make more direct comparisons with the literature and experimental results, future work shall include the extension of the model to Mg and other elements with non-ideal axial ratio. In the case of the fcc structure, this would entail using a hexagonal unit cell rather than a cubic one and changing the axial ratio from ideal to the desired value, obtaining an orthorombic structure. This research would constitute a further check of the validity of the model. The same process could be carried out to calculate the SFEs of the alloys and compare them directly with the literature. In addition, the SFEs of crystals with higher alloy concentration could be calculated, as well as those of some ternary alloys.

As a method to calculate SFEs, the ANNI model and its extensions present undoubted advantages. In particular, this model is highly efficient when compared to the supercell method: only the perfect structures are required, and small cells can be used, lowering significantly the computational cost of the calculation, as well as improving convergence. Moreover, the energies of the four faults can be calculated at the same time from a limited number of perfect structures, without the need to complicate the geometry of the cell. On the other hand, the drawbacks of this method include the impossibility to localise the stacking faults inside the structure; this prevents us from analysing the effect of placing alloying elements near or away from the fault. Overall, the present work suggests that the $AN(N)^NI$ model is useful tool to gain insight on the properties of crystals, and that it would be an interesting object of further studies.

REFERENCES

[1] Magnesium Elektron. Designing with Elektron Magnesium Alloys, 2012.

[2] International Magnesium Association. Medical Applications. `http://www.intlmag.org/page/app_medical_ima`, 2018. (Accessed: 15-03-2018).

[3] Ding Zhigang, S Li, W Liu, and Yonghao Zhao. Modeling of Stacking Fault Energy in Hexagonal-Close-Packed Metals. 2015, 05 2015.

[4] W. Kohn and L. J. Sham. Self-Consistent Equations Including Exchange and Correlation Effects. Phys. Rev., 140:A1133–A1138, Nov 1965.

[5] N. Chetty and M. Weinert. Stacking faults in magnesium. Phys. Rev. B, 56:10844–10851, Nov 1997.

[6] A. Kelly and G.W. Groves. Crystallography and crystal defects. Engineering Series. Addison-Wesley, 1970.

[7] M.T. Dove. Structure and Dynamics: An Atomic View of Materials. Oxford Master Series in Condensed Matter Physics 1. OUP Oxford, 2003.

[8] S. H. Simon. The Oxford Solid State Basics. Oxford University Press, 1 edition, 8 2013.

[9] P. Hofmann. Solid State Physics: An Introduction, 2nd Edition. Wiley, 2 edition, 4 2015.

[10] J.P. Hirth and J. Lothe. Theory of Dislocations. Krieger Publishing Company, 1982.

[11] L. S. Ramsdell. Studies on Silicon Carbide. Am. Mineral 132, pages 64–82, 1945.

[12] T. Ayalew. 2.1.1 Crystallography. `http://www.iue.tuwien.ac.at/phd/ayalew/node20.html`. (Accessed: 31-10-2017).

[13] D.L. Medlin, G.H. Campbell, and C.B. Carter. Stacking defects in the 9r phase at an incoherent twin boundary in copper. Acta Materialia, 46(14):5135 – 5142, 1998.

[14] D. Farkas, S. J. Zhou, C. Vailh, B. Mutasa, and J. Panova. Embedded atom calculations of unstable stacking fault energies and surface energies in intermetallics. Journal of Materials Research, 12(1):9399, 1997. doi:10.1557/JMR.1997.0015.

[15] P J H Denteneer and W van Haeringen. Stacking-fault energies in semiconductors from first-principles calculations. Journal of Physics C: Solid State Physics, 20(32):L883, 1987.

[16] J. Selinger. Introduction to the Theory of Soft Matter. Springer, 2 edition, 2016.

[17] J. Yeomans. The Theory and Application of Axial Ising Models. volume 41 of Solid State Physics, pages 151 – 200. Academic Press, 1988.

[18] Qing-Miao Hu and Rui Yang. Basal-plane stacking fault energy of hexagonal close-packed metals based on the Ising model. Acta Materialia, 61(4):1136 – 1145, 2013.

[19] A. F. Wright. Basal-plane stacking faults and polymorphism in AlN, GaN, and InN. Journal of Applied Physics, 82(10):5259–5261, 1997.

[20] R.G. Parr and Y. Weitao. Density-Functional Theory of Atoms and Molecules. International Series of Monographs on Chemistry. Oxford University Press, 1989.

[21] M. Finnis. Interatomic Forces in Condensed Matter. EBSCO ebook academic collection. Oxford University Press, 2003.

[22] A. T. Paxton. Electronic Structure, Course Notes. King's College London, 1995. URL \url{https://www.kcl.ac.uk/nms/depts/physics/people/academicstaff/paxton.aspx}.

[23] C. C. J. Roothaan. New Developments in Molecular Orbital Theory. Rev. Mod. Phys., 23:69–89, Apr 1951.

[24] P. Hohenberg and W. Kohn. Inhomogeneous Electron Gas. Phys. Rev., 136:B864–B871, Nov 1964.

[25] M. Methfessel. Multipole Green functions for electronic structure calculations. PhD thesis, Katholike Universiteit te Nijmegen, 1986.

[26] Questaal. `https://www.questaal.org/`, 2018. (Accessed: 24-02-2018).

[27] E. Bott, M. Methfessel, W. Krabs, and P. C. Schmidt. Nonsingular Hankel functions as a new basis for electronic structure calculations. Journal of Mathematical Physics, 39(6):3393–3425, 1998.

[28] M. Methfessel, M. van Schilfgaarde, and R. A. Casali. A Full-Potential LMTO Method Based on Smooth Hankel Functions. 09 1999.

[29] O. K. Andersen. Linear methods in band theory. Phys. Rev. B, 12:3060–3083, Oct 1975.

[30] Takao Kotani and Mark van Schilfgaarde. Fusion of the LAPW and LMTO methods: The augmented plane wave plus muffin-tin orbital method. Phys. Rev. B, 81, Mar 2010.

[31] John P. Perdew, Kieron Burke, and Matthias Ernzerhof. Generalized Gradient Approximation Made Simple. Phys. Rev. Lett., 77:3865–3868, Oct 1996.

[32] E. I. Andritsos, G. C. G. Skinner, and A. T. Paxton. Effect of Ca on the Microstructure and Mechanical Properties in Mg Alloys. In Dmytro Orlov, Vineet Joshi, Kiran N. Solanki, and Neale R. Neelameggham, editors, Magnesium Technology 2018, pages 63–69, Cham, 2018. Springer International Publishing.

[33] M. Y. Chou, Marvin L. Cohen, and Steven G. Louie. Theoretical study of stacking faults in silicon. Phys. Rev. B, 32:7979–7987, Dec 1985.

[34] M. Methfessel and A. T. Paxton. High-precision sampling for Brillouin-zone integration in metals. Phys. Rev. B, 40:3616–3621, Aug 1989.

[35] Peter E. Blöchl, O. Jepsen, and O. K. Andersen. Improved tetrahedron method for Brillouin-zone integrations. Phys. Rev. B, 49:16223–16233, Jun 1994.

[36] Brillouin zone integration. https://www.questaal.org/docs/numerics/bzintegration/#comparing-sampling-to-tetrahedron-integration, 2018. (Accessed: 11-03-2018).

[37] K. Lejaeghere, V. Van Speybroeck, G. Van Oost, and S. Cottenier. Error Estimates for Solid-State Density-Functional Theory Predictions: An Overview by Means of the Ground-State Elemental Crystals. Critical Reviews in Solid State and Materials Sciences, 39(1):1–24, 2014.

[38] L. Wen, P. Chen, Z.-F. Tong, B.-Y. Tang, L.-M. Peng, and W.-J. Ding. A systematic investigation of stacking faults in magnesium via first-principles calculation. The European Physical Journal B, 72(3):397, Nov 2009.

[39] A.E. Smith. Surface, interface and stacking fault energies of magnesium from first principles calculations. Surface Science, 601(24):5762 – 5765, 2007. Wagga Symposium on Surfaces and Interfaces - 2006.

[40] Binglun Yin, Zhaoxuan Wu, and W.A. Curtin. Comprehensive first-principles study of stable stacking faults in hcp metals. Acta Materialia, 123:223 – 234, 2017.

[41] P. E. Blöchl. Projector augmented-wave method. Phys. Rev. B, 50:17953–17979, Dec 1994.

[42] Yue Wang and John P. Perdew. Correlation hole of the spin-polarized electron gas, with exact small-wave-vector and high-density scaling. Phys. Rev. B, 44:13298–13307, Dec 1991.

[43] Xiaozhi Wu, Rui Wang, and Shaofeng Wang. Generalized-stacking-fault energy and surface properties for HCP metals: A first-principles study. Applied Surface Science, 256(11):3409 – 3412, 2010.

[44] S. Sandlöbes, M. Frik, S. Zaefferer, A. Dick, S. Yi, D. Letzig, Z. Pei, L.-F. Zhu, J. Neugebauer, and D. Raabe. The relation between ductility and stacking fault energies in Mg and MgY alloys. Acta Materialia, 60(6):3011 – 3021, 2012.

[45] Y. Wang, L.-Q. Chen, Z.-K. Liu, and S.N. Mathaudhu. First-principles calculations of twin-boundary and stacking-fault energies in magnesium. Scripta Materialia, 62(9):646 – 649, 2010.

[46] Md Mezbahul Islam, Ahmad Mostafa, and Mamoun Medraj. Essential Magnesium Alloys Binary Phase Diagrams and Their Thermochemical data. 2014:33, 04 2014.

[47] J. Harris. Simplified method for calculating the energy of weakly interacting fragments. Phys. Rev. B, 31: 1770–1779, Feb 1985.

[48] W. Matthew C. Foulkes and Roger Haydock. Tight-binding models and density-functional theory. Phys. Rev. B, 39:12520–12536, Jun 1989.

[49] A J Read and R J Needs. Tests of the harris energy functional. Journal of Physics: Condensed Matter, 1

(41):7565.

[50] H. M. Polatoglou and M. Methfessel. Comparison of the Harris and the Hohenberg-Kohn-Sham functionals for calculation of structural and vibrational properties of solids. Phys. Rev. B, 41:5898–5903, Mar 1990.

[51] M. van Schilfgaarde, A.T. Paxton, A. Pasturel, and M. Methfessel. Recent Advances in Non Self-Consistent Total Energy Calculations in Alloys. MRS Proceedings, 186:107, 1990.

[52] M. Muzyk, Z. Pakiela, and K.J. Kurzydlowski. Generalized stacking fault energy in magnesium alloys: Density functional theory calculations. Scripta Materialia, 66(5):219 – 222, 2012.

[53] Joseph A. Yasi, Louis G. Hector, and Dallas R. Trinkle. First-principles data for solid-solution strengthening of magnesium: From geometry and chemistry to properties. Acta Materialia, 58(17):5704 – 5713, 2010.

[54] Quan Zhang, Lin Fu, Tou-Wen Fan, Bi-Yu Tang, Li-Ming Peng, and Wen-Jiang Ding. Ab initio study of the effect of solute atoms Zn and Y on stacking faults in Mg solid solution. Physica B: Condensed Matter, 416:39 – 44, 2013.

[55] E. I. Andritsos. Stacking fault energies of Mg binary alloys. Unpublished, 2018.

[56] S.L. Shang, W.Y. Wang, B.C. Zhou, Y. Wang, K.A. Darling, L.J. Kecskes, S.N. Mathaudhu, and Z.K. Liu. Generalized stacking fault energy, ideal strength and twinnability of dilute Mg-based alloys: A first-principles study of shear deformation. Acta Materialia, 67:168 – 180, 2014.

[57] William Yi Wang, Shun Li Shang, Yi Wang, Zhi-Gang Mei, Kristopher A. Darling, Laszlo J. Kecskes, Suveen N. Mathaudhu, Xi Dong Hui, and Zi-Kui Liu. Effects of Alloying Elements on Stacking Fault Energies and Electronic Structures of Binary Mg Alloys: A First-Principles Study. Materials Research Letters, 2(1):29–36, 2014.